Bulletin of the Seismological Society of America, Vol. 107, No. 5, pp. 2353–2366, October 2017, doi: 10.1785/0120170009

Probabilistic Seismic-Hazard Assessment for East Anatolian Fault Zone Using Planar Fault Source Models

by Zeynep Gülerce, Syed Tanvir Shah, Akın Menekşe, Atilla Arda Özacar, Nuretdin Kaymakci, and Kemal Önder Çetin

Abstract The objective of this article is to provide state-of-the-art probabilistic seismic-hazard assessment maps for the East Anatolian fault zone (EAFZ) based on planar seismic-source models and up-to-date ground-motion models. Development of fault-based seismic-source models requires the definition of source geometry in terms of fault length, fault width, fault-plane angles, and segmentation points for each segment of the EAFZ, building rupture systems that consider fault-to-fault ruptures and associating the observed seismicity with defined rupture systems. This complicated task was performed by compiling the seismotectonic characteristics of the EAFZ using available geological information and the instrumental earthquake catalogs of Turkey. Recently published global Next Generation Attenuation (NGA)-West2 ground-motion models (Bozorgnia *et al.*, 2014) and Turkey-adjusted NGA-West1 models (Gülerce *et al.*, 2016) are used in the ground-motion logic tree with equal weights. The results are presented in terms of the seismic-hazard maps for hazard levels in design codes for different spectral periods and for rock-like reference site conditions ($V_{S30} = 760$ and 1100 m/s).

Introduction

Three major structures govern the active tectonics of Turkey: the dextral North Anatolian fault zone (NAFZ), the sinistral East Anatolian fault zone (EAFZ), and the slab-edge processes related to the Aegean–Cyprian subduction system in the eastern Mediterranean (Fig. 1a). Among these fault systems, the NAFZ is responsible for the largest earthquake rupture sequence in the last century (eight $M_w > 6.7$ events between 1939 and 1999). Especially after the 1999 M_w 7.52 Kocaeli and M_w 7.2 Düzce events, a number of studies providing the seismic hazard and risk estimates along the NAFZ and/or in the Marmara region have been published (e.g., Atakan *et al.*, 2002; Erdik *et al.*, 2004; Crowley and Bommer, 2006; Kalkan *et al.*, 2009; Gülerce and Ocak, 2013). The EAFZ, the other intracontinental transform fault that translates the Anatolian plate westward toward the Aegean–Cyprian subduction system, had seismically been quiet relative to the NAFZ in the twentieth century. It has generally been neglected in terms of probabilistic seismic-hazard assessment (PSHA) studies, except for the country-wide works of Erdik *et al.* (1985, 1999) and Gülkan *et al.* (1993). In these extensively used national PSHA studies, areal source zones with homogenous spatial seismicity distribution were preferred, and the activity rates were calculated based on the seismicity in each zone. In the most recent European PSHA effort, the Seismic Harmonization in Europe (SHARE) project (see Data and Resources), both areal source zones and planar fault sources were developed for the NAFZ and EAFZ and combined in the logic tree. Both in the areal source model and the fault source and background model (FSBG), the magnitude recurrence was modeled by double-truncated Gutenberg–Richter relation; however, activity rates were calculated considering the geodetic and geological constraints in the FSBG model (Woessner *et al.*, 2015).

Gülerce and Vakilinezhad (2015) showed that the design ground motions estimated by PSHA using areal source zones are significantly smaller than the results of PSHA based on planar fault models in the close vicinity of the NAFZ. Therefore, planar fault-source models that properly represent the complexities in the fault geometry and accumulation of the seismic moment should be developed for the NAFZ and EAFZ. Over the past 5 yrs, a substantial amount of data related to the seismotectonic characteristics of the EAFZ has been published. The official active fault maps of Turkey (in 1:25,000) were updated by the General Directorate of Mineral Research and Exploration of Turkey (MTA, Emre *et al.*, 2013). Moreover, Duman and Emre (2013) documented the geometry and segmentation characteristics of the northern and southern strands of EAFZ. In addition, a number of studies related to the geological characteristics and displacement rates of the different segments of the EAFZ have been published (e.g., Yılmaz *et al.*, 2006; Bulut *et al.*, 2012; Koç and

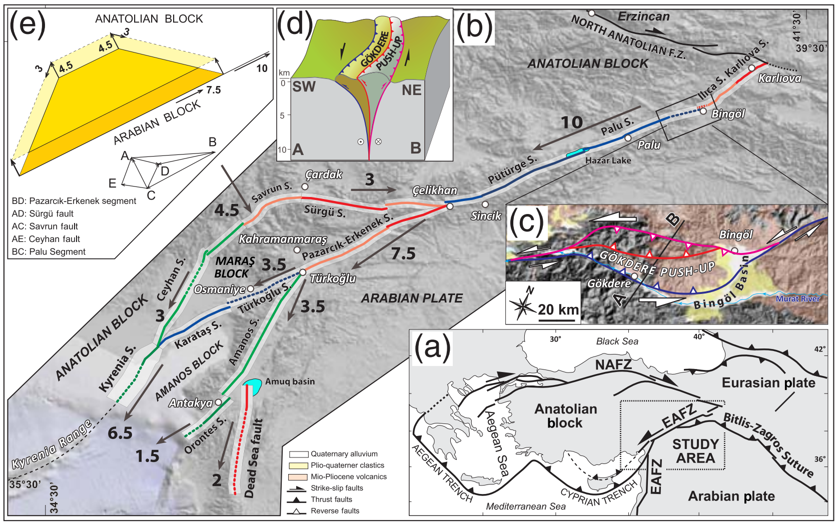

Figure 1. (a) Simplified active tectonic scheme of Turkey (modified from Kaymakci *et al.*, 2007) EAFZ, East Anatolian fault zone; NAFZ, North Anatolian fault zone. (b) Major branches of EAFZ and slip rates based on geological and Global Positioning System (GPS) velocities. Solid lines are after Emre *et al.* (2013). Dashed lines are used in this study based on our compilations. (c) Blow-up map, and (d) 3D geometry of Gökdere push-up. (e) Vector summation used to calculate the slip vectors for the faults defining the Maraş block. The color version of this figure is available only in the electronic edition.

Kaymakcı, 2013; Mahmoud *et al.*, 2013; Bayrak *et al.*, 2015; Emre *et al.*, 2016).

In this regard, the main objective of this contribution is to update the design ground motions and the seismic-hazard maps of the region around the EAFZ using planar fault-source models that combine the recently published information on source geometry and fault kinematics. In developing the planar seismic-source models, the activity rate for each rupture source is calculated using the relationship between the accumulated seismic moment (due to the slip rate on the fault) and released seismic moment. The step-by-step procedure of building the fault-based seismic-source models is provided in the next section. The ground-motion characterization logic tree of this study includes recently developed Next Generation Attenuation (NGA)-West2 ground-motion models (GMMs) (Bozorgnia *et al.*, 2014) and the Turkey (TR)-adjusted NGA-West1 (Gülerce *et al.*, 2016) models that were regionalized based on Turkish strong-motion database. These GMMs are briefly introduced, and the logic-tree weights are given in the Ground-Motion Characterization section. The PSHA Maps for the EAFZ and the Comparison with the Previous PSHA Maps section presents and discusses the seismic-hazard maps for peak ground acceleration (PGA). Two sets of PGA maps for two hazard levels and two different rock-site conditions, $V_{S30} = 760$ m/s, representing the B/C boundary of the National Earthquake Hazards Reduction Program (NEHRP) site classification scheme (Building Seismic Safety Council, 2004), and $V_{S30} = 1100$ m/s, to provide the reference rock-site conditions that might be used in site-specific response analysis, are provided.

Seismic Source Characterization (SSC) Models for the EAFZ

The EAFZ is a northeast–southwest (NE–SW)-striking left-lateral intracontinental strike-slip fault system that extends between the Karlıova junction (where it meets the NAFZ) and Antakya at the NE corner of the Mediterranean Sea (Şaroğlu *et al.*, 1992). The transform nature of the EAFZ was first recognized by Arpat and Şaroğlu (1972), and later the seismotectonic characteristics of the fault zone has been studied by numerous researchers (e.g., McKenzie, 1972, 1976, 1978; Arpat and Şaroğlu, 1975; Jackson and McKenzie, 1984; Dewey *et al.*, 1986; Ambraseys, 1989; Taymaz *et al.*, 1991; Lyberis *et al.*, 1992; Westaway and Arger, 1996; Westaway, 2003, 2004). A comprehensive summary of the previous literature on the geological and tectonic characteristics of the EAFZ is provided in Duman and Emre (2013); therefore, only the issues that significantly affect the SSC model developed for this study are elaborated here. The SSC model proposed herein mostly adopts the fault lines given in the updated active fault maps of MTA (Emre *et al.*, 2013), which are digitized for their geometry and termination points of segments (solid lines in Fig. 1b). However, additional segments that are not available in Emre *et al.* (2013) are considered (or available segments are extended). These additions are indicated by dashed lines in Figure 1b, and each addition is described in this section, starting from NE to SW.

Karlıova and Ilıca segments of the EAFZ extend from the Karlıova triple junction in the NE and continue southwestward to the east of Bingöl (Şaroğlu and Yılmaz, 1990). The area is characterized by notable seismic activity, including the 1866 M_s 7.0 Karlıova (Ambraseys and Jackson, 1998) and the 22 May 1971 M_s 6.8 Bingöl earthquakes. We adopted the fault segments given in Emre *et al.* (2013) from Karlıova to Bingöl. The continuation of the EAFZ between the northeastern corner of Bingöl Plain and Palu is very diffuse (Fig. 1). Here, the EAFZ is bifurcated into a number of branches that mostly have the combination of sinistral strike-slip and reverse-slip components. The deformation styles in the region are characterized by a typical compressional duplex geometry (terminology after Woodcock and Fischer, 1986), which is named as the Gökdere restraining bend by Duman and Emre (2013) and the Gökdere push-up herein. The Gökdere push-up is about a 50-km-long and 25-km-wide spindle-shaped positive area with a typical push-up geometry (Fig. 1c,d). Three fault segments control the Gökdere push-up; two of them define its northern and southern boundaries, whereas one of the segments is approximately collinear with the general trend of the EAFZ and dissects the push-up into two blocks. Duman and Emre (2013) reported that the southern edge of the bend is bounded by the Murat River, which was tectonically incised to depths of 700–1000 m during the Quaternary time (Şaroğlu *et al.*, 1992). Possibly, this margin is a strike-slip fault with a south-verging reverse component. Herece (2008) reported ~600 m uplift of the push-up based on elevated terrace deposits during the Quaternary. In the north, the push-up is delimited by a strike-slip fault with a north-verging reverse component, and the eastern margin is delimited by the Bingöl pull-apart basin. In the northwest, faults related to the continuation of the Palu segment merge with the bend and are transformed into thrust faults (Duman and Emre, 2013). Arpat (1971) and Arpat and Şaroğlu (1972) reported up to 1.8-km-long surface ruptures related to the 1971 Bingöl earthquake in the region. Although $M_w > 4$ events were observed in this region during the instrumental period, fault lines given for the Ilıca and Palu segments in the updated active fault maps of MTA (Emre *et al.*, 2013) are discontinuous near the Gökdere push-up. Thus, the system is characterized as a positive flower structure controlled by a vertical strike-slip fault crossing the Gökdere push-up, which forms the western continuation of Ilıca segment in this study (Fig. 1d).

One of the contentious issues in developing the SSC models for the EAFZ is the continuation of the EAFZ toward the west from Türkoğlu. Some authors suggested that the EAFZ continues westward from Türkoğlu and connects with the Türkoğlu–Karataş fault zone and further west into the Kyrenia Range in Cyprus (McKenzie, 1976; Gülen *et al.*, 1987; Hempton, 1987; Karig and Kozlu, 1990; Perinçek and Çemen, 1990, Westaway and Arger, 1996; Westaway, 2003). Others follow the proposal of Şaroğlu *et al.* (1992) that the EAFZ extends southward from Türkoğlu and reaches the Amuq basin through the Amanos fault (Herece, 2008; Karabacak *et al.*, 2010; Duman and Emre, 2013). Meghraoui *et al.* (2009) proposed that the EAFZ bifurcates into two branches: the SW–NE-striking Karataş–Osmaniye (KO) and the south-southwest–north-northeast-striking Karasu faults based on Global Positioning System (GPS) measurements and the analysis of fault kinematics data around the Kahramanmaraş–Hatay region. In our analyses, we included both the Türkoğlu–Karataş and Amanos branches in the earthquake rupture forecast as parallel segments that share the total slip rate (Fig. 1b). The Türkoğlu–Karataş rupture system has not been connected to the Türkoğlu junction by Emre *et al.* (2013), therefore, as part of this study, the northern end of the fault up to the Türkoğlu junction is extended following the fault maps provided by McKenzie (1976), Hempton (1987), and Westaway and Arger (1996). The Türkoğlu–Karataş and Amanos rupture systems defined in this study match with the KO and Karasu faults proposed by Westaway (2003) and Meghraoui *et al.* (2011).

The most significant difference between Emre *et al.* (2013) and this study comprises the kinematics and southwestern continuation of the Sürgü fault zone (SFZ). The SFZ is regarded as a sinistral strike-slip fault in Emre *et al.* (2013). However, Koç and Kaymakcı (2013) argued that the SFZ is a dextral shear zone based on field observations, fault-slip data, and morphotectonic observations, such as displaced and skewed stream courses along the fault zone, indicating dextral motion for more than 3 km. They proposed that the characteristics of the fault zone changes as the trace of the master fault changes along strike. It is a dextral strike-slip fault zone in the east and gradually acquires a reverse component westward as the fault trace curves southward, forming a restraining bend. Further west, it becomes a reverse fault, especially along the Savrun segment. In this study, the proposal of Koç and Kaymakcı (2013) is followed for the fault kinematics, but the fault zone is subdivided into two rupture systems. The eastern system includes the dextral Sürgü rupture system, and it includes the fault segments from the EAFZ in the east up to a point where the fault makes a sharp southward bend around Çardak (Fig. 1b).

Koç and Kaymakcı (2013) stated that the eastern section of the Savrun fault has a reverse component, due to the bending of the fault system. Consistently, the fault is modeled as a reverse and single-segment rupture system independently from the Sürgü rupture system. Because there are controversies about the style of faulting (SoF) for the Savrun fault, a set of sensitivity analysis had been performed by changing the SoF parameter (as strike slip and reverse) and the dip angle of the fault (90° for strike slip and 45°–70° for reverse) in Menekşe (2016). Sensitivity analysis results showed that the dip angle and SoF did not have a significant effect on the hazard results for near-fault sites: the variations on the estimated PGA values were less than 5% for the 475 yr return period. As the source-to-site distance increases, decreasing the dip angle increases the estimated PGA values, especially for higher-hazard levels. When the dip angle is selected as 70° to represent the oblique character of the Savrun segment (as suggested by Koç and Kaymakcı, 2013), the choice of SoF parameter does not significantly change the design PGA values in the near field.

Some of the fault lines given in Emre *et al.* (2013) are extended as shown by the dashed lines in Figure 1b. The southwestern continuation of the Savrun fault is named here as the Ceyhan fault, a large part of which is included in Emre *et al.* (2013) as the Misis fault. The fault is exposed within the basement rocks, but so far there is no surface rupture mapped along the fault, which is one of the main criteria in Emre *et al.* (2013) for a fault to be classified as an active fault. This fault was recognized and mapped by Perinçek *et al.* (1987) as part of the Göksu fault zone. Later, Yalçınkaya (2005) related its activity to the 27 June 1998 Ceyhan earthquake, and Kaymakci *et al.* (2010) provided information about kinematics of the fault. We extended the exposed fault segments below the alluvium and indicated the extended part as a dashed line in Figure 1b to complete the fault-block model. In this study, the Ceyhan fault is modeled as the western boundary fault of the Maraş block, and its slip rate is constrained accordingly (Fig. 1e). In Emre *et al.* (2013), only the on-land faults are provided. We extended the southwestern end of the Karataş fault into the offshore area based on the Misis–Kyrenia fault zone of Aksu *et al.* (2005). Similarly, the Dead Sea fault is shown up to the Turkish–Syrian border by Emre *et al.* (2013). The Hacıpaşa fault of Karabacak *et al.* (2010) is used as the northernmost segment of the Dead Sea fault zone in Turkey.

Definition of Rupture Systems and the Segmentation Model

A key concern in the SSC model is the definition of fault segmentation models for the earthquake rupture forecast. Several studies proposed different segmentation models for the EAFZ based on different criteria. Hempton *et al.* (1981) suggested five segments based on the geometrical properties of the fault plane and changes in the fault trend, whereas Barka and Kadinsky-Cade (1988) defined 14 distinct segments, due to the discontinuities (stepovers) along the master fault trace and the relationship between previous surface ruptures and earthquake activity. In Şaroğlu *et al.* (1992), the EAFZ was divided into six segments based on fault stepovers and changes in the strike of the master fault trace, assuming that the segments can move separately along their lengths, independent of the adjacent segments. A similar approach was adopted in the recent work of Duman and Emre (2013). They proposed seven segments, with segment lengths ranging between 31 and 113 km for the master fault strand. The fault-segmentation model proposed by Duman and Emre (2013) had been adopted in the updated active fault maps of the MTA (Emre *et al.*, 2013).

Recent large-magnitude earthquakes (e.g., the 2002 Denali and 2010 El Mayor–Cucapah earthquakes) showed that the fault ruptures may be complex and span multiple connected fault segments, even if the segments are separated by distinct geological and geomorphological features on the surface (Haeussler *et al.*, 2004; Fletcher *et al.*, 2014). To be able to consider multiple-segment ruptures in the rupture forecast, the segmentation model proposed by Duman and Emre (2013) for the main strand of the EAFZ is simplified by merging some of the neighboring segments. As a result, three distinct and nonoverlapping segments (or rupture systems) are defined between Karlıova and Türkoğlu: the Ilıca–Karlıova, Palu, and Pazarcık–Erkenek rupture systems, as shown in Figure 1b. The Ilıca–Karlıova rupture system includes the Karlıova and Ilıca segments defined by Duman and Emre (2013), in addition to the western continuation of the Ilıca segment delineated in the Gökdere push-up.

Şaroğlu *et al.* (1992) defined two separate segments lying in between Palu and Lake Hazar (the Palu segment of Duman and Emre, 2013) and Lake Hazar and Sincik (the Pütürge segment of Duman and Emre, 2013), separated by the Lake Hazar releasing bend. The authors proposed that these segments "can be separated where a pull-apart basin reflected by Lake Hazar is formed, otherwise the two segments are continuous and hence during an earthquake, they may move together" (p. 112). A recent study in the Lake Hazar basin, constrained by high-resolution seismic data combined with land-based observations and analysis of geophysical and geological data from Lake Hazar, revealed that the main strand of the the EAFZ is continuous across the Hazar basin (Garcia Moreno *et al.*, 2011). In the region, both recorded seismicity (Fig. 2) and fault orientations support a continuous single rupture system. Thus, the Palu and Pütürge segments that have been treated previously as two separate systems are combined into one large rupture system in this study to avoid any possible underestimation of seismic hazard.

The relationship between the Pazarcık and Erkenek segments is also controversial. Lovelock (1984), Lyberis *et al.* (1992), and Chorowicz *et al.* (1994) argued that no major active strike-slip faults are present in the Gölbaşı area. On the contrary, McKenzie (1976), Dewey *et al.* (1986), Perinçek *et al.* (1987), Barka and Kadinsky-Cade (1988), and Perinçek and Çemen (1990) suggested that the EAFZ is continuous through the the Gölbaşı basin. Interpretations by Biricik (1994), Westaway and Arger (1996), and Güneyli (2008) suggest that the Gölbaşı basin is a classical pull-apart basin that has been developed between the Pazarcık and Erkenek segments. Yılmaz *et al.* (2006) performed a fault-kinematics study along this segment and concluded that the Neogene stress configurations in the region showed a distinct strike-slip character with a reverse component, and most likely the same stress conditions were still active until recently, as indicated by seismicity; therefore, we combined the Pazarcık and Erkenek segments as the the Pazarcık–Erkenek rupture system.

Even though the smaller segments given in Duman and Emre (2013) are combined into relatively bigger rupture systems, the changes in the fault-plane trend, fault jogs, and discontinuities are taken into consideration in PSHA by dividing the rupture systems into smaller fault segments. These small segments are used as the basic building blocks for the earthquake-rupture forecast. The methodology used in this study was outlined in the (Working Group on California Earthquake Probabilities [WGCEP], 2003) San Francisco Bay area model. In WGCEP (2003), a fault segment is defined as the shortest fault section capable of rupturing repeatedly to produce large earthquakes. Both geometric (along-strike variations of fault geometry, presence of fault bends, oversteps, and jogs, etc.), kinematic, and dynamic (information about previous events which includes timing of events, slip rate, rupture length, and distribution of seismic activity) criteria can be used to delimit the fault segments. The fault segments defined for the EAFZ are presented in the third column of Table 1. The rupture source is defined as single or multiple adjacent fault segments that may rupture and produce an earthquake in the future. Any possible combination of sources that describes the full rupture of the system is defined as the rupture scenario by WGCEP (2003). The fault-rupture model includes the weighted combination (weighted average) of all rupture scenarios for the rupture system.

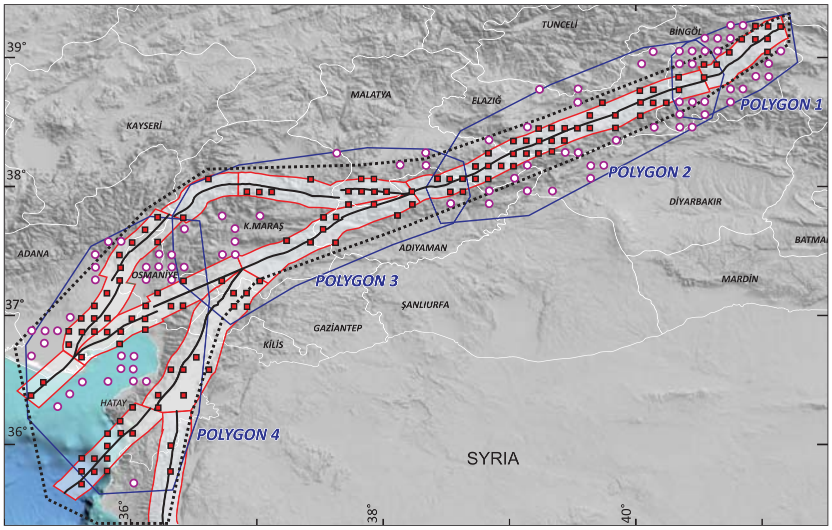

Figure 2. Rupture systems and the instrumental seismicity ($M_w \geq 4$). The buffer zones used for source-to-epicenter matching are shown around the rupture systems. Small boxes show the earthquakes associated with the rupture systems; whereas, all seismicity (both small boxes and circles) are used to calculate the *b*-values. Solid lines are the polygons used for calculating the *b*-values. Dashed lines delimit the area of the whole polygon used in calculating the EAFZ-specific *b*-value. The color version of this figure is available only in the electronic edition.

Magnitude Distribution Model Parameters

After the fault geometry models and rupture systems are defined, the rupture models are built by following these steps: (1) selection of the proper magnitude probability distribution functions (PDFs) and definition of the model parameters, (2) estimating the activity rates and forming the magnitude-recurrence model based on the annual slip rate and selected magnitude PDF (the moment-balancing approach as defined by Hecker *et al.*, 2013), (3) association of the seismicity with the defined rupture systems, and (4) testing the magnitude-recurrence model based on the associated catalog seismicity.

Hecker *et al.* (2013) and Gülerce and Vakilinezhad (2015) showed that coupling the truncated exponential magnitude PDF with seismic sources defined by planar fault geometries results in unrealistically high rates for small-to-moderate magnitude events. Therefore, the composite magnitude PDF proposed by Youngs and Coppersmith (1985) is preferred to represent the relative rates of small-, moderate-, and large-magnitude earthquakes for each rupture source. The composite magnitude PDF includes three parameters: the minimum magnitude (M_{min} is defined as M_w 4.0 for all seismic sources based on the magnitude of catalog completeness and considering the magnitude limit below which the earthquake has no impact on the structure), characteristic magnitude (M_{char}), and the *b*-value (slope of the line that represents relative frequency of small-to-moderate earthquakes). Median M_{char} values for each segment are calculated by the magnitude–rupture area relationships proposed by Wells and Coppersmith (1994; hereafter, WC94) and Hanks and Bakun (2014; hereafter, HB14) for strike-slip faults and are listed in Table 1. In these calculations, the fault width for each rupture system were back-calculated from the rupture zones of previous large-magnitude events when possible (e.g., for the 1822 Antakya, 1971 Bingöl, and 2010 Palu earthquakes), and the calculated fault-width values are in good agreement with the depth values given in Emre *et al.* (2016). The difference in the estimated median M_{char} using WC94 and HB14 equations is not very significant (less than 0.1 magnitude unit for all segments). Therefore, the median M_{char} values based on WC94 equations are preferred and used in the developed SSC model by assigning a weight of 0.6 in the logic tree (a weight of 0.2 is assigned to the median $\pm 1\sigma$ values each, in which σ is approximately equal to the WC94 standard deviation in magnitude units). The upper bounds for the magnitude PDF (M_{max}) are determined by adding a magnitude unit of 0.25 to the M_{char} for each branch in the logic tree (Fig. 3).

The Integrated and Homogeneous Turkish Earthquake Catalog (Kalafat *et al.*, 2011), including the events with $M_w \geq 4$ that occurred between 1900 and 2010, is utilized to represent the instrumental-era seismicity in the region. This catalog is enriched by 41 additional events with $M_w \geq 4$ that occurred between 2011 and 2014 in the region, and their M_w values are computed from local magnitudes, using magnitude-conversion equations proposed by Akkar *et al.* (2010). After the magnitude scales are unified, the aftershocks and mainshocks are declustered (aftershocks are removed), based on the method proposed by Reasenberg (1985) using the ZMAP software package (Wiemer, 2001), with minimum and maximum look-ahead times of 1 and 10 days, respectively, and an event-crack radius of 10 km. The *b*-values are calculated within the large-scaled polygons defined around the rupture systems (shown in Fig. 2), using the maximum-likelihood estimation (MLE) and the weighted least-squares (WLS) regression (Aki, 1965; Utsu, 1965; Wiemer and Wyss, 1997) (Table 2). Figure 4a–e shows that the completeness magnitude (M_c) and the *b*-value for polygons 1–5, estimated by the MLE and WLS methods, are in good agreement, except for polygon 1 (covering a larger area around the Karlıova–Ilıca segments). The lowest *b*-value is obtained for the Ilıca–Karlıova rupture system, indicating that the Ilıca–Karlıova region has higher stress levels than the others. It is worth noting that polygon 1 had the least number of earthquakes and thus can be more affected by temporary changes in stress conditions. To minimize the possible effects related to undersampling and/or temporary changes, both the rupture system-specific *b*-values and the *b*-value calculated for the whole EAFZ are employed, with equal weights assigned in the SSC logic tree (Table 2 and Fig. 3).

Table 1
The Fault Segments and the Rupture Systems Included in the Seismic Source Characterization (SSC) Model

Rupture System Number	Rupture System Name	Segment Name	Length (km)	Width (km)	Slip Rate (mm/yr)	WC94 M_{char} (M_w)	HB14 M_{char} (M_w)
1	Ilıca–Karlıova	Ilıca	32.45	15	10	6.72	6.67
1	Ilıca–Karlıova	Karlıova	40.95	15	10	6.82	6.79
2	Palu	Palu1	101.11	15	10	7.22	7.28
2	Palu	Palu2	93.54	15	10	7.19	7.23
2	Palu	Palu3	30.03	15	10	6.69	6.63
3	Pazarcık–Erkenek	Pazarcık	83.17	15	7.5	7.14	7.17
3	Pazarcık–Erkenek	Erkenek	52.30	15	7.5	6.93	6.92
4	Amanos	Amanos	140.98	15	3.5	7.37	7.45
5	Türkoğlu–Karataş	Karataş	71.52	15	3.5	7.07	7.09
5	Türkoğlu–Karataş	Türkoğlu	68.96	15	3.5	7.05	7.07
6	Sürgü	Sürgü 1	48.86	15	3.0	6.90	6.88
6	Sürgü	Sürgü 2	69.93	15	3.0	7.06	7.08
7	Savrun	Sürgü West (Savrun)	56.82	15	4.5	6.97	6.96
8	Ceyhan	Ceyhan	105.56	15	3.0	7.24	7.30
8	Ceyhan	Kozan	42.59	15	3.0	6.84	6.81
9	Kyrenia	Kyrenia	66.79	15	6.5	7.04	7.05
10	Orontes	Orontes	53.76	15	1.5	6.94	6.93
11	Dead Sea fault	Dead Sea fault	194.56	15	2.0	7.51	7.63

WC94, Wells and Coppersmith (1994); HB14, Hanks and Bakun (2014).

Slip Portioning along the Proposed Segmentation Model and Moment-Balancing Procedure

For each rupture source, the activity rate is calculated by combining the magnitude-distribution model by the balance between the accumulated and released seismic moments, as shown in equation (1). The accumulated seismic moment is a function of the annual slip rate (s) in cm/yr, the area of the fault (in cm^2), and the shear modulus of the crust (μ in dyn/cm^2). In the following equation, $f_m(M_w)$ represents the composite magnitude PDF of Youngs and Coppersmith (1985):

$$N(\mathrm{M}) = \frac{\mu \mathrm{AS}}{\int_{M_{\min}}^{M_{\max}} f_m(M_w) 10^{1.5M_w+16.05} dm} \int_{M_{\min}}^{M_{\max}} f_m(M_w) d_M. \quad (1)$$

The annual slip rate has a significant impact on the activity rates calculated by equation (1). McClusky *et al.* (2000) and Reilinger *et al.* (2006) proposed a 10 mm/yr slip rate for the master strand of the EAFZ (between Çelikhan and Karlıova), based on GPS measurements. This well-established value for the annual slip rate for the EAFZ is adopted. Because the motion of the Maraş block is due northwestward away from the Arabian plate (Fig. 1e), the relative motion along the Pazarcık–Erkenek rupture system is decreased. The annual slip rate along this rupture system is calculated as 7.5 mm/yr, based on the block model given in Figure 1e. This value is consistent with the slip rate proposed by Duman and Emre (2013) for the Erkenek segment. The annual slip rate proposed by Koç and Kaymakcı (2013) for the Sürgü and Savrun rupture systems (2 mm/yr) is modified for a better fit with the released seismic moment based on associated seismicity. A 3 mm/yr dextral slip rate is assigned on the Sürgü rupture system, converted to 4.5 mm/yr slip rate over the dipping plane for the Savrun rupture system and 3 mm/yr sinistral slip along the Ceyhan rupture system (Fig. 1b).

Various interpretations on the annual slip rate are available for the region to the south of the Türkoğlu junction in the current literature. In this study, the Türkoğlu–Karataş and Amanos rupture systems are considered in the earthquake-rupture forecast as conjugate fault segments, and the kinematics of these segments are determined by the motion of the Amanos block, which is well constrained by GPS studies (Reilinger *et al.*, 2006). In the block models proposed by Mahmoud *et al.* (2013), the total slip rate (varying between 6.5 and 8.2 mm/yr, depending on the defined blocks) is equally shared among the KO and Karasu faults. Similarly, equal slip rates are assigned (3.5 mm/yr) to the Türkoğlu–Karataş and Amanos rupture systems. Further south, the Amanos segment bifurcates into two branches around the Amuq valley. One of the segments, the Orontes fault, trends SW, whereas the other segment strikes north–south and constitutes the northernmost extent of the Dead Sea fault zone. The slip rate of the Dead Sea fault in this region is around 2 mm/yr (Reilinger *et al.*, 2006; Alchalbi *et al.*, 2010), indicating that the slip along the Orontes segment must be approximately equal to 1.5 mm/yr.

The appropriateness of the selected magnitude PDF and the accuracy of the model parameters (i.e., *b*-value, slip rate, or M_{max}) will be tested by the relative frequency of the seismicity associated with the source in the moment-balanced PSHA procedure. Associating the catalog seismicity with defined rupture systems might be challenging, especially when the distance between the parallel fault strands is relatively small. Bulut *et al.* (2012) stated that the observed seismicity generally follows the trend of the EAFZ along a 20-km-wide stripe, except for the Çelikhan area, where off-fault distances of seismicity clusters are larger. To perform the source-to-

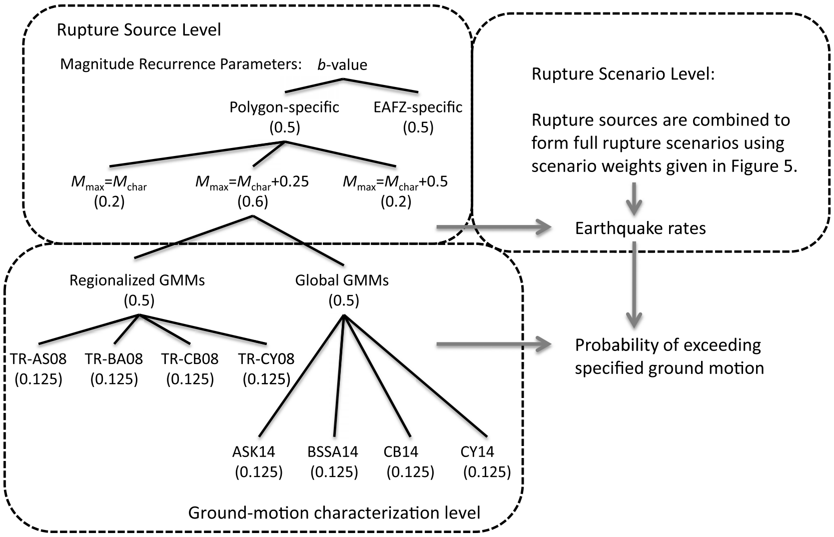

Figure 3. Logic tree used in the probabilistic seismic-hazard assessment (PSHA) calculations. GMMs, ground-motion models; TR, Turkey. ASK14, Abrahamson *et al.* (2014); BSSA14, Boore *et al.* (2014); CB14, Campbell and Bozorgnia (2014); CY14, Chiou and Youngs (2014); TR-AS08, TR-BA08, TR-CB08, and TR-CY08 are the TR-adjusted versions of Abrahamson and Silva (2008); Boore and Atkinson (2008); Campbell and Bozorgnia (2008); Chiou and Youngs (2008) GMMs, respectively.

epicenter matching, 10-km-wide (5 km in each side of the fault) buffer zones are created around the rupture systems, and the epicenters located within the buffer zones are assumed to be the earthquakes originated from that particular rupture system. In Figure 2, small boxes show the earthquakes associated with the rupture systems, whereas all seismicity (both small boxes and circles) are used to calculate the *b*-values. For the Amanos rupture system, the buffer zone is slightly widened to 12 km to capture the extensional stepover structure in the the Karasu valley. After the EAFZ master strand splits into branches at Türkoğlu, small modifications are made on the buffer zones, depending on the geometry of the parallel branches and the distribution of the seismicity.

After the source-to-epicenter matching is completed, a weight is assigned to each rupture scenario, and the cumulative rates of events attributed to that particular rupture system are plotted, along with the weighted average of the rupture scenarios, to calibrate the assigned weights and to evaluate the balance of the accumulated and released seismic moment. The moment-balancing graphs for the Ilıca–Karlıova, Palu, Pazarcık–Erkenek, Türkoğlu–Karataş, Amanos, Sürgü, Ceyhan, and Dead Sea fault (DSF) rupture systems are provided in Figure 5. In these plots, black dots stand for the cumulative annual rates of earthquakes, and error bars represent the uncertainty introduced by unequal periods of observation for different magnitudes (Weichert, 1980). The best fit between the cumulative annual rate of events and the weighted average of rupture scenarios (dotted lines) is established by modifying the weights of the rupture scenarios and the parameters of the composite magnitude PDF.

In Figure 5, the scenarios that are separated by plus signs in the legend are the scenarios with multiple rupture sources. When multiple segments rupture together, these scenarios are separated by a comma sign in the legend. For example, the "Ilıca + Karlıova" line in Figure 5a represents the scenario in which the Ilıca and Karlıova segments are ruptured individually. This scenario brings in relatively higher rates for small-to-moderate earthquakes when compared with the "Ilıca, Karlıova" scenario which represents the rupture of these two segments together to produce a larger event. In each moment-balancing plot, relatively higher weights are assigned to the rupture scenarios that combine the individual (single-segment) rupture sources, based on the assumption that single-segment ruptures are more likely than multiple-segment ruptures. The weights assigned to each rupture scenario are shown in parenthesis in Figure 5, and these values are adopted in the logic tree. None of the scenarios are discarded by assigning an insignificant (or zero) weight in the moment-balancing procedure.

Ground-Motion Characterization

In PSHA, the GMMs are used to estimate the ground-motion parameters based on the earthquake scenarios from each source. There are major uncertainties associated with both the SSC models and the GMMs in the PSHA framework, but the uncertainties associated with the latter will generally have the larger impact on the results (Bommer *et al.*,

Table 2
b-Values Estimated Using Different Methods and Corresponding Weights in the Logic Tree

	Maximum-Likelihood Estimation (MLE)		Weighted Least-Square (WLS)		Manual Fit in ZMAP	
Region	*b*-Value	Weight	*b*-Value	Weight	*b*-Value	Weight
EAFZ_Whole polygon	0.81	0.167	0.848	0.167	0.9	0.166
Polygon 1 (Karlıova–Ilıca)	0.632	0.25	0.578	0.25	—	—
Polygon 2 (Palu)	0.715	0.25	0.745	0.25	—	—
Polygon 3 (Pazarcık–Erkenek, Sürgü, Savrun)	0.918	0.25	0.913	0.25	—	—
Polygon 4 (Ceyhan, Türkoğlu– Karataş, Amanos, Kyrenia, Orontes, DSF)	0.86	0.25	0.875	0.25	—	—

EAFZ, East Anatolian fault zone; DSF, Dead Sea fault.

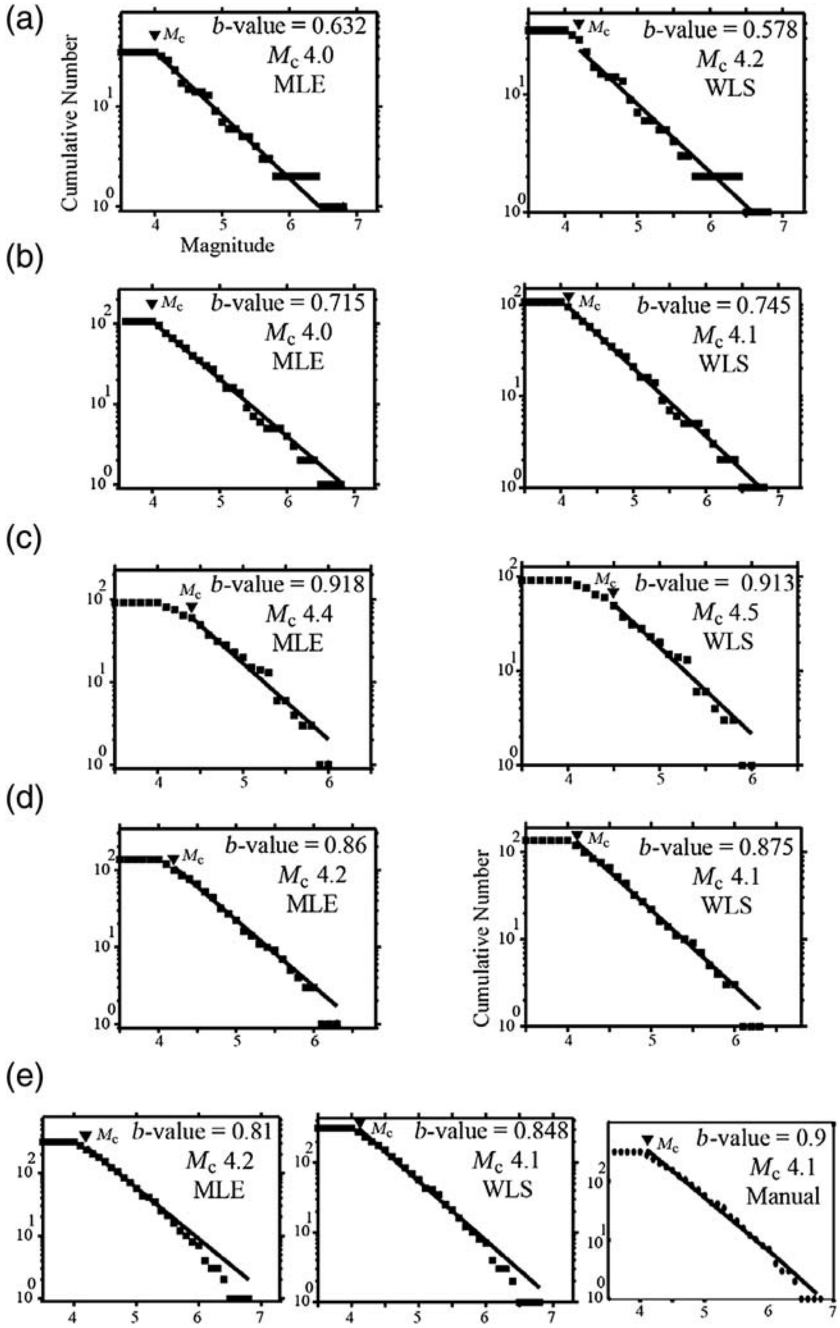

Figure 4. Completeness magnitude (M_c) and the *b*-value for defined polygons calculated by the maximum-likelihood estimation (MLE) and weighted least-squares (WLS) regression; (a) polygon 1, (b) polygon 2, (c) polygon 3, (d) polygon 4, and (e) the EAFZ whole polygon. For the last (and the largest) polygon, the manually fitted line is also provided. For the geographic extents of the polygons, refer to Figure 2.

2005; Vakilinezhad *et al.*, 2013). Constructing the GMM logic tree for PSHA applications is a controversial issue because local GMMs are developed from the regional datasets, so they are expected to reflect the regional tectonic characteristics better than the others, but the uncertainties introduced by local GMMs are higher than those of the global GMMs because they are based on statistically less stable and limited datasets. GMMs that are suitable for PSHA studies in Turkey are thoroughly discussed in Gülerce *et al.* (2016), with a focus on NGA-West1 (Power *et al.*, 2008) and NGA-West2 (Bozorgnia *et al.*, 2014) models and their performance on predicting the ground motions in the Turkish ground-motion dataset (Akkar *et al.*, 2010). Findings of Gülerce *et al.* (2016) are considered for constructing the GMM logic tree in this study. Because the details are provided in the original reference, only a brief summary is given here.

Gülerce *et al.* (2016) used the plots of the interevent and intraevent residuals to evaluate the differences in the magnitude, distance, and site-amplification scaling between the Turkish strong-ground-motion dataset and the NGA-West1 models. Distribution of interevent residuals indicated that the ground motions in the Turkish strong-motion dataset are overestimated by the NGA-West1 models. This discrepancy is corrected by modifying (only) the small-to-moderate magnitude scaling of the NGA-West1 GMMs to preserve the well-constrained large-magnitude scaling of the global models. Magnitude corrections applied to the NGA-West1 models are in good agreement with the magnitude scaling of NGA-West2 GMMs with more flexible functional forms (Campbell and Bozorgnia, 2014, hereafter, CB14 and Chiou and Youngs, 2014, hereafter, CY14 models) in the $5 < M_w < 6.75$ range. For smaller magnitudes ($M_w < 4$), predictions of the NGA-West2 models and the TR-adjusted NGA-West1 models are similar. The updated model by (Idriss, 2014; hereafter, ID14) has approximately the same magnitude scaling with the NGA-West1 version (Idriss, 2008; hereafter, ID08), and both models are significantly different than the TR-adjusted version of the Idriss (2008) model (TR-ID08). Therefore, the models proposed by Idriss (2008, 2014) are excluded from the GMM logic tree for this study. Gülerce *et al.* (2016) pointed out that the mean bias in the median predictions of the TR-ID08 model remained for the long periods even after the adjustments; therefore, the TR-adjusted version of the ID08 model is excluded, and all other TR-adjusted NGA-West1 models (TR-AS08, TR-BA08, TR-CB08, and TR-CY08, the TR-adjusted versions of Abrahamson and Silva, 2008; Boore and Atkinson, 2008; Campbell and Bozorgnia, 2008; Chiou and Youngs, 2008, GMMs, respectively) are included in the GMMs logic tree.

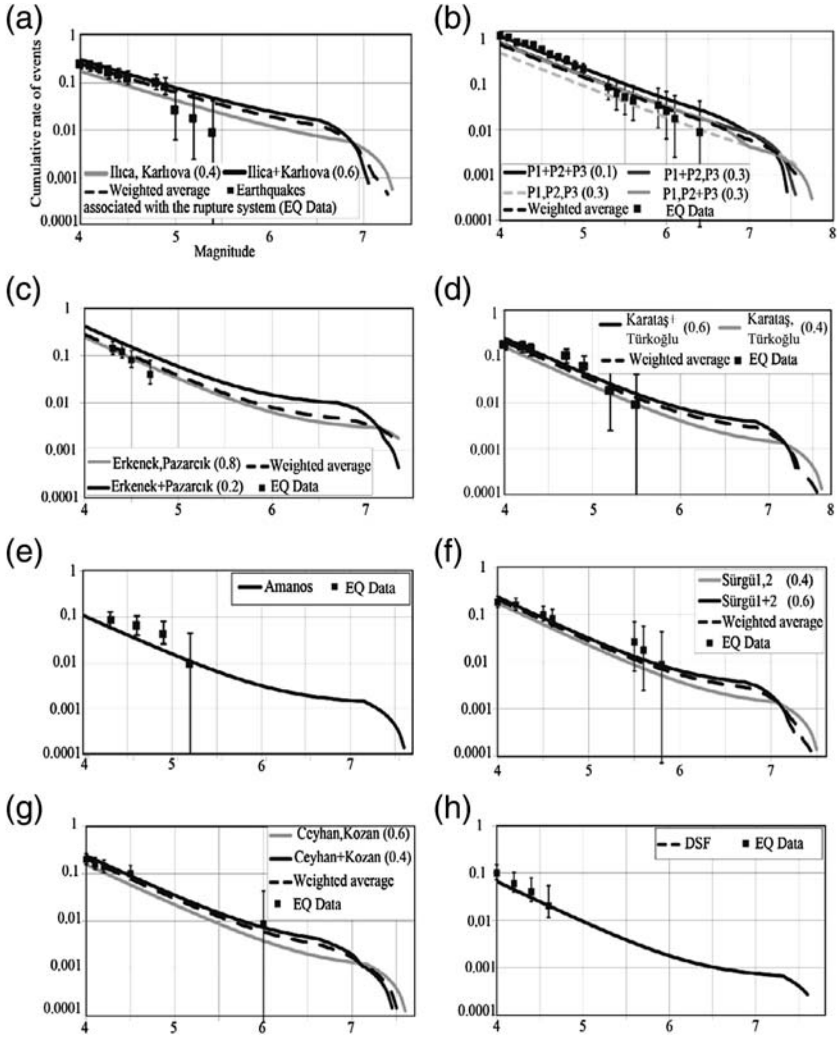

Figure 5. Cumulative rates of associated earthquakes and proposed magnitude-recurrence models for (a) the Ilıca–Karlıova, (b) the Palu, (c) the Pazarcık–Erkenek, (d) the Türkoğlu–Karataş, (e) the Amanos, (f) the Sürgü, (g) the Ceyhan, and (h) the Dead Sea fault (DSF) rupture systems.

The suite of the NGA-West2 models was found to provide median ground-motion predictions that agree with each other within the factors of about 1.5–2. The biggest differences are observed for the cases in which the NGA-West2 database is incomplete, such as for large earthquakes ($M_w > 7.5$) at close distances and for hanging-wall sites located over the rupture plane of shallow-dipping earthquakes. Therefore, all NGA-West2 models, except for the ID14 model, are included in the GMM logic tree to properly represent the epistemic uncertainty. The selected four TR-adjusted NGA-West1 models and four NGA-West2 models (Abrahamson *et al.*, 2014, hereafter, ASK14; Boore *et al.*, 2014, with regional adjustment applied to anelastic attenuation for Turkey, hereafter, BSSA14; Campbell and Bozorgnia, 2014, and Chiou and Youngs, 2014) were implemented individually in the preliminary hazard runs to quantify the effect of GMM selection on the hazard outcome, and the results are elaborated in Menekşe (2016). Because there are no systematic differences between the hazard estimates of selected models in the high-frequency and low-frequency ranges, equal weights are assigned to the models in the logic tree (12.5% for each model, Fig. 3). Further analysis of the model predictions with recently developed techniques, such as the high-dimensional visualization approach (Scherbaum *et al.*, 2010), trellis charts for global (Stewart *et al.*, 2015) and site-specific (Zimmaro and Stewart, 2017) applications might be considered for the logic-tree weights of selected GMMs but are not applied in this study.

PSHA Maps for the EAFZ and Comparison with the Previous PSHA Maps

The Cornell–McGuire PSHA methodology (Cornell, 1968; McGuire, 2004) was adopted, and the numerical integration of the hazard integral is performed, using the computer code HAZ45 (Pacific Gas & Electric Company [PG&E], 2010). HAZ45 treats the epistemic uncertainties in the SSC models and the GMMs through the use of logic trees. For each rupture source, all combinations of the logic-tree branches are evaluated. For estimating the total hazard on a site, Monte Carlo sampling of source characterization uncertainty is used to combine the epistemic uncertainty for each rupture source. Additionally, full sampling of the GMMs is used to develop the fractals on the total hazard. To prepare the seismic-hazard maps, 653 grid points are defined around the EAFZ, and the density of the grid points is increased within the close vicinity of the fault plane for accuracy (Menekşe, 2016). The last set of points in the grid is 33 km away from the fault plane. Additionally, two different rock-site conditions, rock 1 being the B/C boundary in the NEHRP-site classification system ($V_{S30} = 760$ m/s) and rock 2 being the reference rock-site conditions to be used in site-specific response analysis ($V_{S30} = 1100$ m/s), are defined for each site (Choi and Stewart, 2005; Walling *et al.*, 2008). Based on the PSHA results, seismic-hazard maps for PGA and spectral accelerations at $T = 0.2$ and 1.0 s, corresponding to the return periods of 475 yrs (10% chance of exceedance at 50 yrs) and 2475 yrs (2% chance of exceedance at 50 yrs) around the EAFZ for rock 1 and rock 2 site conditions are prepared.

The seismic-hazard maps for the 475-yr and 2475-yr return period PGA are shown in Figures 6 and 7, respectively. In both maps, the PGA contours closely follow the fault

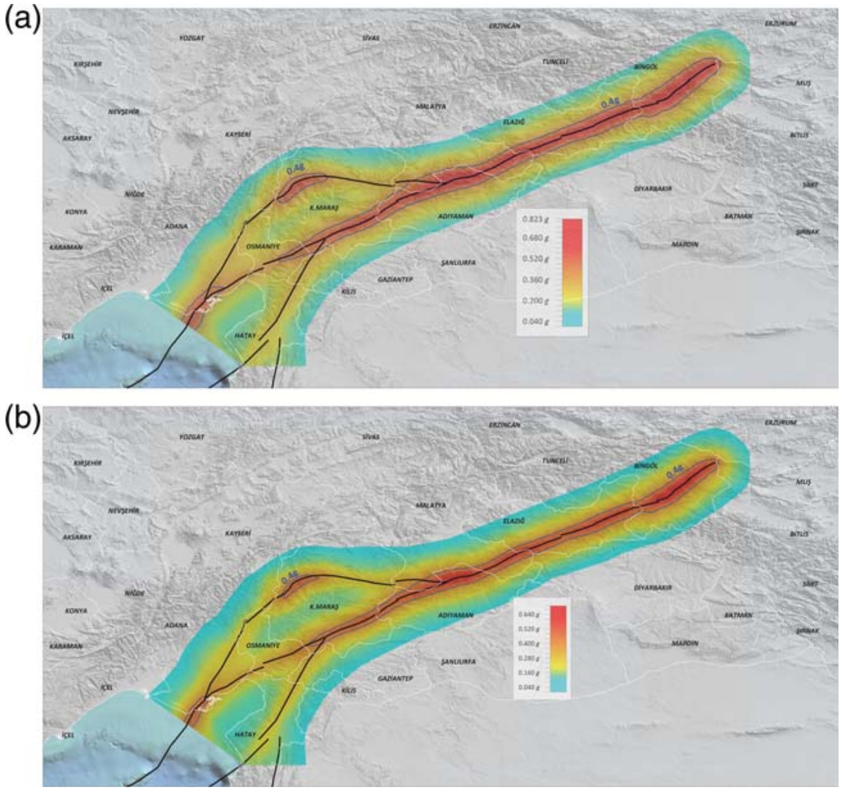

Figure 6. PSHA map for the 475-yr return period peak ground acceleration (PGA) for (a) $V_{S30} = 760$ m/s and (b) $V_{S30} = 1100$ m/s. Contour lines (for PGA $= 0.4g$) represent the design value for the highest earthquake zone in Turkish Earthquake Code (2007). The color version of this figure is available only in the electronic edition.

lines, as expected. As the source-to-site distance increases, estimated ground-motion values attenuate quite rapidly. The highest ground motions are estimated in the vicinity of the Palu rupture system, for which the assigned annual slip rate is the highest (10 mm/yr) and the b-value is the lowest among the other rupture systems. The maximum value of the 475-yr return period PGA is $0.82g$ for rock 1 conditions and $0.64g$ for rock 2 site conditions. As the hazard level increases, the design ground motions also increase considerably. The maximum 2475-yr return period PGA value is equal to $1.25g$ and $1.0g$ for rock 1 and rock 2 site conditions, respectively. Estimated values are comparable with the recently proposed ground-motion estimates around the NAFZ. The maximum 2475-yr return period PGA in the Marmara region was found to be between $1.5g$ and $1.65g$ by Erdik *et al.* (2004), Kalkan *et al.* (2009), and Gülerce and Ocak (2013) for $V_{S30} = 760$ m/s. The values estimated around the NAFZ are higher than the ones estimated around the EAFZ, even if the segment lengths and fault activity in both fault zones are comparable, because the annual slip rate of the the NAFZ is up to two times higher than that of the EAFZ.

The seismic-hazard maps proposed by previous studies (e.g., Erdik *et al.*, 1999, and the SHARE project in Woessner *et al.*, 2015) are quite similar to the results obtained in this study, especially along the master strand of the EAFZ between Karlıova and Türkoğlu. There is a narrowband around the fault at which the 475-yr return period PGA values are higher than $0.6g$ in Erdik *et al.* (1999), higher than $0.5g$ in SHARE, and $0.7g$ in Figure 6a. This high-PGA zone in the previous PSHA maps is larger and more homogenous than the high-PGA zone shown in Figures 6 and 7, due to the fact that the seismicity was uniformly distributed in the areal source zones around the EAFZ in previous attempts. Because the activity of the northern strand of the EAFZ was only recently acknowledged, the PGA values for the 475-yr return period estimated in this study around the the Sürgü, Savrun, and Ceyhan rupture systems are significantly higher than the PGA values given in previous maps. There is a substantial reduction in the PGA values on the south of the Gölbaşı juncture in the SHARE hazard map, indicating that the decrease in the annual slip rate of the Amanos rupture system (probably due to the slip-rate participation between the Amanos rupture system and the other tectonic structures in the area) was also considered in the SHARE project SSC model.

According to the zonation map of the Turkish Earthquake Code (2007; hereafter, TEC-2007), the EAFZ master strand (until the south of the Amanos rupture system) is situated in the earthquake-hazard zone for which the design PGA is equal to $0.4g$ for regular buildings and $0.6g$ for important structures (zone I). Contours of PGA $= 0.4g$ and $0.6g$ are given for comparison in Figures 6 and 7, respectively. Both of these figures clearly show that the PGA $> 0.4g$ and PGA $> 0.6g$ zones of the proposed maps are mostly concentrated around the master strand of the EAFZ but quite thin when compared with the first-degree earthquake-hazard zone of TEC-2007. The design PGA values are higher than $0.4g$ within the ± 15 km buffer zone around the fault plane only up to the south of Türkoğlu. Areas with PGA $> 0.4g$ are rarely observed at the south of this point, except for two patches: the area around the Savrun fault with thrust component and at the intersection of the Ceyhan and Türkoğlu–Karataş rupture systems. It should be noted that the southern parts of the Türkoğlu–Karataş and Ceyhan rupture systems, in addition to the Sürgü and Kyrenia rupture systems, are located in zone II and that the Savrun rupture system is located in zone III, according to the TEC-2007 zonation map, in which the design PGA $= 0.3g$ and $0.2g$, respectively.

Summary and Conclusions

The PSHA framework and its components adopted by this study reflect a significant step forward in the PSHA

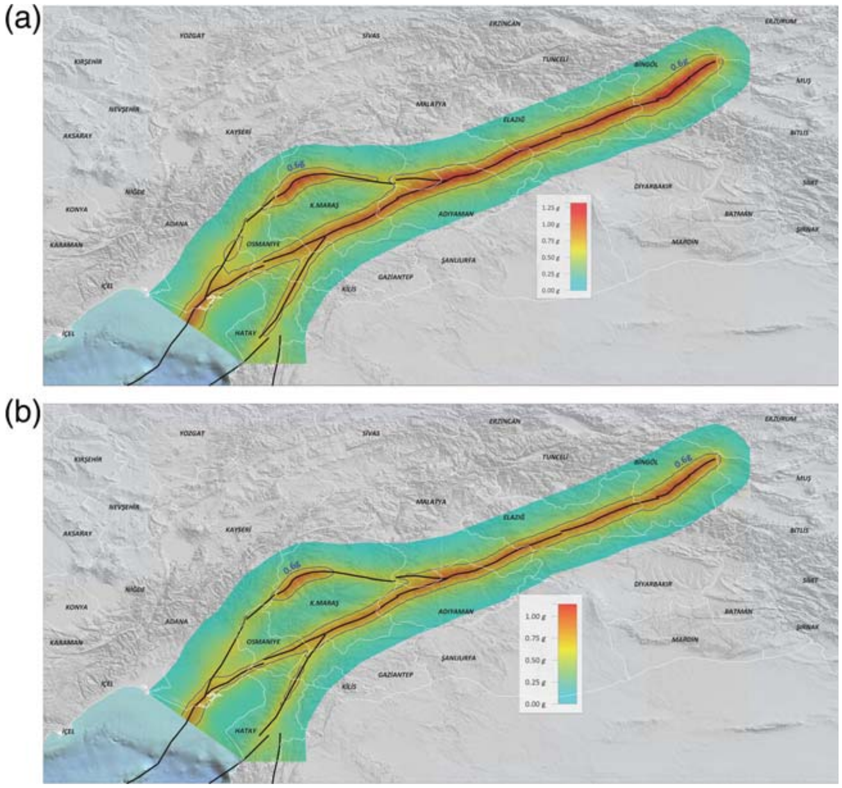

Figure 7. PSHA map for the 2475-yr return period PGA for (a) $V_{S30} = 760$ m/s and (b) $V_{S30} = 1100$ m/s. Contour lines (for PGA $= 0.6g$) represent the design value for special structures for the highest earthquake zone in Turkish Earthquake Code (2007). The color version of this figure is available only in the electronic edition.

The SSC model developed here does not include any floating seismic sources to model the earthquakes that may occur outside the buffer zones around the fault planes. Contribution of other nearby active tectonic structures, such as the Bitlis–Zagros suture zone and the NAFZ, is neglected. Therefore, the PSHA maps proposed in this study underestimate the hazard at the northeastern tip of the EAFZ, on the east of the Gölbaşı, and in the area that lies in between the Türkoğlu–Karataş and Amanos rupture systems. The annual slip-rate partitioning between the parallel segments of the EAFZ on the south of the Türkoğlu juncture is still under debate, and this distribution has a significant effect on our results. Proper evaluation of associated slip rates on these parallel segments by GPS measurements and state-of-the-art block models will reduce the uncertainty in these parameters and will lead to more-accurate estimation of design ground-motion levels. Presence of aseismic deformation or creep along the EAFZ is still enigmatic. The preliminary analysis of InSAR and GPS data along the Hazar–Palu section of the EAFZ provided evidence for aseismic deformation comparable with long-term slip rate (Çetin *et al.*, 2016), but the extent of the creeping zones and their rates is not yet well constrained along the EAFZ, thus excluded from further analysis in this study. The recurrence intervals for the characteristic event for any segment of the EAFZ are not available; therefore, time-dependent hazard methodologies are not employed in this study. Determination of paleoseismic recurrence periods will provide a substantial contribution in the PSHA practice of Turkey and eventually will lead to a decrease in the hazard estimates when the time-dependent methods are utilized. We did not build alternative source models as in Uniform California Earthquake Rupture Forecast, version 3 (UCERF3; Field *et al.*, 2014), even if we apply the traditional logic-tree approach for the magnitude recurrence parameters including the maximum magnitudes. For controversial issues (e.g., combination of the segments given in Emre *et al.*, 2013, or participation of the slip rates in parallel branches), our decisions are always biased toward the alternatives that result in higher hazard outputs.

practice of Turkey. The SSC model developed for this study does not combine the areal sources with homogenous seismicity (or buffer zones or background sources) with the planar fault sources by any means. Instead, planar fault sources that account for the geological constraints and the relative rates of small-, moderate-, and large-magnitude events are built based on the most current seismotectonic information. The rupture sources presented here do not represent the earthquakes outside the buffer zones. In site-specific applications, these rupture systems may be combined with gridded seismicity zones to account for the possible off-the-fault seismicity. The GMMs employed in this study (NGA-West2 and the TR-adjusted NGA-West1 models) represent the state of the art in the global and region-specific ground-motion characterization studies, because these models are slowly being embedded in the PSHA software. Because the SSC models and the ground-motion characterization structure defined here are substantially more diverse than the previous PSHA studies in this region, the amplitude and spatial distribution of the estimated ground motions in this study are different than the earthquake code requirements. The PSHA maps are quite similar to the estimations of Erdik *et al.* (1999) and the SHARE project between Karlıova and Türkoğlu, but significantly different in the south and southwest of Türkoğlu.

Data and Resources

Information related to the seismotectonic model used in the Seismic Harmonization in Europe (SHARE) Project and the hazard maps are obtained from http://www.efehr.org:8080/jetspeed/portal/hazard.psml (last accessed March 2015). The $M_w \geq 4$ earthquake catalog for 2011–2014 is downloaded from http://www.koeri.boun.edu.tr/sismo/2/earthquake-catalog/ (last accessed December 2014).

Acknowledgments

The efforts by Nick Gregor and Norman A. Abrahamson on incorporating the Turkey-adjusted Next Generation Attenuation (NGA)-West1 models in HAZ45 software are gratefully acknowledged. The authors thank Barış Güner for his contribution in the calculation of magnitude-recurrence model parameters. The authors are thankful to Thomas Pratt, John Douglas, and anonymous reviewers for their insightful comments. This study was partially supported by the Pacific Gas & Electric Company Geosciences Department.

References

Abrahamson, N. A., and W. J. Silva (2008). Summary of the Abrahamson & Silva NGA ground motion relations, *Earthq. Spectra* **24,** 67–97.

Abrahamson, N. A., W. J. Silva, and R. Kamai (2014). Summary of the ASK14 ground motion relation for active crustal regions, *Earthq. Spectra* **30,** 1025–1055.

Aki, K. (1965). Maximum likelihood estimate of b in the formula log $N = a - bM$ and its confidence limits, *Bull. Earthq. Res. Inst. Univ. Tokyo* **43,** 237–239.

Akkar, S., Z. Cagnan, E. Yenier, E. Erdogan, M. A. Sandikkaya, and P. Gulkan (2010). The recently compiled Turkish strong motion database: Preliminary investigation for seismological parameters, *J. Seismol.* **14,** 457–479.

Aksu, A. E., T. J. Calon, J. Hall, S. Mansfield, and D. Yasar (2005). The Cilicia–Adana basin complex, eastern Mediterranean: Neogene evolution of an active fore-arc basin in an obliquely convergent margin, *Mar. Geol.* **22,** 121–159.

Alchalbi, A., M. Daoud, F. Gomez, S. McClusky, R. Reilinger, M. A. Romeyeh, A. Alsouod, R. Yassminh, B. Ballani, and R. Darawcheh (2010). Crustal deformation in northwestern Arabia from GPS measurements in Syria: Slow slip rate along the northern Dead Sea fault, *Geophys. J. Int.* **180,** 125–135.

Ambraseys, N. N. (1989). Temporary seismic quiescence: SE Turkey, *Geophys. J. Int.* **96,** 311–331.

Ambraseys, N. N., and J. A. Jackson (1998). Faulting associated with historical and recent earthquakes in the eastern Mediterranean region, *Geophys. J. Int.* **133,** 390–406.

Arpat, A. E. (1971). 22 Mayıs 1971 Bingöl Depremi-On Rapor, *Rept. 4697*, Institute of Mineral Research and Exploration (in Turkish).

Arpat, E., and F. Şaroğlu (1972). *Doğu Anadolu Fayı ile İlgili Bazı Gözlemler ve Düşünceler*, Institute of Mineral Research and Exploration, Ankara, Turkey, 44–50 (in Turkish).

Arpat, E., and F. Şaroğlu (1975). Some recent tectonic events in Turkey, *Bull. Geol. Soc. Turkey* **18,** 91–101.

Atakan, K., A. Ojeda, M. Meghraoui, A. A. Barka, M. Erdik, and A. Bodare (2002). Seismic hazard in Istanbul following the 17 August 1999 İzmit and 12 November 1999 Düzce earthquakes, *Bull. Seismol. Soc. Am.* **92,** 466–482.

Barka, A. A., and K. Kadinsky-Cade (1988). Strike-slip fault geometry in Turkey and its influence on earthquake activity, *Tectonics* **7,** no. 3, 663–684.

Bayrak, E., Ş. Yılmaz, M. Softa, T. Türker, and Y. Bayrak (2015). Earthquake hazard analysis for East Anatolian fault zone, Turkey, *Nat. Hazards* **76,** 1063–1077.

Biricik, A. S. (1994). Gölbaşı depresyonu, *Türk Coğrafya Dergisi* **29,** 53–81 (in Turkish).

Bommer, J. J., F. Scherbaum, H. Bungum, F. Cotton, F. Sabetta, and N. A. Abrahamson (2005). On the use of logic trees for ground-motion prediction equations in seismic-hazard analysis, *Bull. Seismol. Soc. Am.* **95,** 377–389.

Boore, D. M., and G. M. Atkinson (2008). Ground-motion prediction equations for the average horizontal component of PGA, PGV, and 5%-damped PSA at spectral periods between 0.01 s and 10.0 s, *Earthq. Spectra* **24,** 99–139.

Boore, D. M., J. P. Stewart, E. Seyhan, and G. M. Atkinson (2014). NGA-West2 equations for predicting PGA, PGV, and 5% damped PSA for shallow crustal earthquakes, *Earthq. Spectra* **30,** 1057–1085.

Bozorgnia, Y., N. A. Abrahamson, L. Al Atik, T. D. Ancheta, G. M. Atkinson, J. W. Baker, A. Baltay, D. M. Boore, K. W. Campbell, S. J. Chiou, *et al.* (2014). NGA-West2 research project, *Earthq. Spectra* **30,** 973–987.

Building Seismic Safety Council (2004). *NEHRP Recommended Provisions for Seismic Regulations for New Buildings and other Structures (FEMA 450)*, Building Seismic Safety Council, National Institute of Building Sciences, Washington, D.C.

Bulut, F., Y. Ben-Zion, and M. Bohnhoff (2012). Evidence for a bimaterial interface along the Mudurnu segment of the North Anatolian fault zone from polarization analysis of *P* waves, *Earth Planet. Sci. Lett.* **327,** 17–22.

Campbell, K. W., and Y. Bozorgnia (2008). NGA ground motion model for the geometric mean horizontal component of PGA, PGV, PGD and 5% damped linear elastic response spectra for periods ranging from 0.01 to 10 s, *Earthq. Spectra* **24,** 139–173.

Campbell, K. W., and Y. Bozorgnia (2014). NGA-West2 ground motion model for the average horizontal components of PGA, PGV, and 5%-damped linear acceleration response spectra, *Earthq. Spectra* **30,** 1087–1115.

Çetin, S., S. Ergintav, U. Doğan, Z. Çakır, S. Şentürk, H. Karabulut, F. Şaroğlu, W. Julaiti, and H. Özener (2016). Investigation of the creep along the Hazar–Palu section of the East Anatolian fault (Turkey) using InSAR and GPS observations, *European Geosciences General Assembly 2016*, *Geophys. Res. Abstr.* **18,** Abstract EGU2016-3938.

Chiou, B. S. J., and R. R. Youngs (2008). An NGA model for the average horizontal component of peak ground motion and response spectra, *Earthq. Spectra* **24,** 173–215.

Chiou, B. S. J., and R. R. Youngs (2014). Update of the Chiou and Youngs NGA model for the average horizontal component of peak ground motion and response spectra, *Earthq. Spectra* **30,** 1117–1153.

Choi, Y., and J. P. Stewart (2005). Nonlinear site amplification as function of 30 m shear wave velocity, *Earthq. Spectra* **21,** no. 1, 1–30.

Chorowicz, J., P. Luxey, N. Lyberis, J. Carvalho, J. F. Parrot, T. Yürür, and N. Gündoğdu (1994). The Maraş triple junction (southern Turkey) based on digital elevation model and satellite imagery interpretation, *J. Geophys. Res.* **99,** 20,225–20,242.

Cornell, C. A. (1968). Engineering seismic risk analysis, *Bull. Seismol. Soc. Am.* **58,** 1583–1606.

Crowley, H., and J. J. Bommer (2006). Modelling seismic hazard in earthquake loss models with spatially distributed exposure, *Bull. Earthq. Eng.* **4,** 249–273.

Dewey, J. F., M. R. Hempton, W. S. F. Kidd, F. Şaroglu, and A. M. C. Şengör (1986). Shortening of continental lithosphere: The neotectonics of Eastern Anatolia—A young collision zone, in *Collision Tectonics*, M. P. Coward and A. C. Ries (Editors), Vol. 19, Blackwell Scientific Publications, Osney Mead, Oxford, 3–36.

Duman, T. Y., and Ö. Emre (2013). *The East Anatolian Fault: Geometry, Segmentation and Jog Characteristics*, Geological Society London, London, United Kingdom, Special Publications.

Emre, Ö., T. Y. Duman, S. Özalp, H. Elmacı, Ş. Olgun, and F. Şaroğlu (2013). Active fault map of Turkey, Special Publication, Series 30, General Directorate of Mineral Research and Exploration (MTA), Ankara, Turkey.

Emre, Ö., T. Y. Duman, S. Özalp, F. Şaroğlu, Ş. Olgun, H. Elmacı, and T. Çan (2016). Active fault database of Turkey, *Bull. Earthq. Eng.* 1–47, doi: 10.1007/s10518-016-0041-2.

Erdik, M., B. Y. Alpay, T. Onur, K. Sesetyan, and G. Birgoren (1999). Assessment of earthquake hazard in Turkey and neighbouring regions, *Ann. Geofisc.* **42,** 1125–1138.

Erdik, M., M. Demircioglu, K. Sesetyan, E. Durukal, and B. Siyahi (2004). Earthquake hazard in Marmara region, Turkey, *Soil Dynam. Earthq. Eng.* **24,** 605–631.

Erdik, M., V. Doyuran, N. Akkas, and P. Gulkan (1985). A probabilistic assessment of the seismic hazard in Turkey, *Tectonophysics* **117,** 295–344.

Field, E. H., R. J. Arrowsmith, G. P. Biasi, P. Bird, T. E. Dawson, K. R. Felzer, D. D. Jackson, K. M. Johnson, T. H. Jordan, C. Madden, *et al.* (2014). Uniform California earthquake rupture forecast, version 3 (UCERF3)-The time-independent model, *Bull Seismol. Soc. Am.* **104,** 1122–1180.

Fletcher, J. M., O. J. Teran, T. K. Rockwell, M. E. Oskin, K. W. Hudnut, K. J. Mueller, R. M. Spelz, S. O. Akciz, E. Masana, G. Faneros, *et al.* (2014). Assembly of a large earthquake from a complex fault system: Surface rupture kinematics of the 4 April 2010 El Mayor–Cucapah (Mexico) $M_w = 7.2$ earthquake, *Geosphere* **10,** 797–827.

Garcia Moreno, D., A. Hubert-Ferrari, J. Moernaut, J. G. Fraser, X. Boes, M. Van Daele, U. Avsar, N. Çağatay, and M. De Batist (2011). Structure and recent evolution of the Hazar basin: A strike-slip basin on the East Anatolian fault, eastern Turkey, *Basin Res.* **23,** 191–207, doi: 10.1111/j.1365-2117.2010.00476.x.

Gülen, L., A. Barka, and M. N. Toksoz (1987). Kıtaların çarpışması ve ilgili komplex deformasyon: Maraş üçlü eklemi ve çevre yapıları, *Yerbilimleri* **14,** 319–336 (in Turkish).

Gülerce, Z., and S. Ocak (2013). Probabilistic seismic hazard assessment of eastern Marmara region, *Bull. Earthq. Eng.* **11,** 1259–1277.

Gülerce, Z., and M. Vakilinezhad (2015). Effect of seismic source model parameters on the probabilistic seismic hazard assessment results: A case study for North Anatolian fault zone, *Bull. Seismol. Soc. Am.* **105,** 2808–2822.

Gülerce, Z., B. Kargıoğlu, and N. A. Abrahamson (2016). Turkey-adjusted NGA-West1 horizontal ground motion prediction models, *Earthq. Spectra* **32,** 75–100.

Gülkan, P., M. S. Yucemen, A. Kocyigit, V. Doyuran, and N. Basoz (1993). Seismic zoning map of Turkey based on most recent input, *Middle East Technical University, Earthquake Engineering Research Center, Rept. 93-01*.

Güneyli, H. (2008). Paleo-seismicity of the Golbasi-Turkoğlu segment of the East Anatolian fault system, *TUBITAK Project Rept. 104Y157*.

Haeussler, P., D. P. Schwartz, T. E. Dawson, H. D. Stenner, J. J. Lienkaemper, B. Sherrod, F. Cinti, P. Montone, P. Craw, A. Crone, *et al.* (2004). Surface rupture and slip distribution of the Denali and Totschunda faults in the 3 November 2002 $M_w = 7.9$ earthquake, Alaska, *Bull. Seismol. Soc. Am.* **94,** 25–52.

Hanks, T. C., and W. H. Bakun (2014). M-logA models and other curiosities, *Bull. Seismol. Soc. Am.* **104,** 2604–2610.

Hecker, S., N. A. Abrahamson, and K. E. Wooddell (2013). Variability of displacement at a point: Implications for earthquake-size distribution and rupture hazard on faults, *Bull. Seismol. Soc. Am.* **103,** 651–674.

Hempton, M. R. (1987). Constraints on Arabian plate motion and extensional history of the Red Sea, *Tectonics* **6,** 687–705.

Hempton, M. R., J. F. Dewey, and F. Şaroğlu (1981). The East Anatolian transform fault: Along strike variations in geometry and behaviour, *Eos Trans. AGU* **62,** 393.

Herece, E. (2008). *Doğu Anadolu Fayı (DAF) Atlası*, Vol. 13, General Directorate of Mineral Research and Exploration, Ankara, Turkey, Special Publications, 359 (in Turkish).

Idriss, I. M. (2008). An NGA empirical model for estimating the horizontal spectral values generated by shallow crustal earthquakes, *Earthq. Spectra* **24,** 217–242.

Idriss, I. M. (2014). NGA-West2 model for estimating average horizontal values of pseudo-absolute spectral accelerations generated by crustal earthquakes, *Earthq. Spectra* **30,** 1155–1177.

Jackson, J., and D. P. Mckenzie (1984). Active tectonics of the Alpine–Himalayan belt between western Turkey and Pakistan, *Geophys. J. Roy. Astron. Soc.* **77,** 185–264.

Kalafat, D., Y. Güneş, K. Kekovali, M. Kara, P. Deniz, and M. Yilmazer (2011). *Bütünleştirilmiş Homojen Türkiye Deprem Kataloğu (1900-2010); M ≥4.0*, Boğaziçi Üniversitesi, Kandilli Rasathanesi ve Deprem Araştırma Enstitüsü, Istanbul, Turkey, Publication Number: 1049, 640 pp. (in Turkish).

Kalkan, E., P. Gulkan, N. Yilmaz, and M. Celebi (2009). Reassessment of probabilistic seismic hazard in the Marmara region, *Bull. Seismol. Soc. Am.* **99,** 2127–2146.

Karabacak, V., E. Altunel, M. Meghraouı, and H. S. Akyüz (2010). Field evidences from northern Dead Sea fault zone (south Turkey): New findings for the initiation age and slip rate, *Tectonophysics* **480,** 172–182.

Karig, D. E., and H. Kozlu (1990). Late Paleogene-Neogene evolution of the triple junction near Maraş, south-central Turkey, *J. Geol. Soc. Lond.* **147,** 1023–1034.

Kaymakci, N., E. Aldanmaz, C. Langereis, T. L. Spell, O. F. Gurer, and K. A. Zanetti (2007). Late Miocene transcurrent tectonics in NW Turkey: Evidence from palaeomagnetism and 40Ar–39Ar dating of alkaline volcanic rocks, *Geol. Mag.* **144,** 379–392.

Kaymakci, N., M. Inceöz, P. Ertepinar, and A. Koç (2010). Late Cretaceous to recent kinematics of SE Anatolia (Turkey), *Geol. Soc. Lond. Spec. Issue* **340,** 409–435.

Koç, A., and N. Kaymakcı (2013). Kinematics of Sürgü fault zone (Malatya, Turkey): A remote sensing study, *J. Geodyn.* **65,** 292–307.

Lovelock, P. E. R. (1984). A review of the tectonics of the northern Middle East region, *Geol. Mag.* **121,** 577–587.

Lyberis, N., T. Yurur, J. Chorowicz, E. Kasapoglu, and N. Gundogdu (1992). The East Anatolian fault: An oblique collisional belt, *Tectonophysics* **204,** 1–15.

Mahmoud, Y., F. Masson, M. Meghraoui, Z. Cakir, A. Alchalbi, H. Yavasoglu, O. Yönlü, M. Daoud, S. Ergintav, and S. Inan (2013). Kinematic study at the junction of the East Anatolian fault and the Dead Sea fault from GPS measurements, *J. Geodyn.* **67,** 30–39.

McClusky, S., S. Balassanian, A. Barka, C. Demir, S. Ergintav, I. Georgiev, O. Gurkan, M. Hamburger, K. Hurst, H. Kahle, *et al.* (2000). Global Positioning System constraints on plate kinematics and dynamics in the Mediterranean and Caucasus, *J. Geophys. Res.* **105,** 5685–5719.

McGuire, R. K. (2004). *Seismic Hazard and Risk Analysis*, Earthquake Engineering Research Institute, Oakland, California, MNO-10.

McKenzie, D. P. (1972). Active tectonics of the Mediterranean region, *Geophys. J. Roy. Astron. Soc.* **30,** 109–185.

McKenzie, D. P. (1976). The East Anatolian fault; a major structure in eastern Turkey, *Earth Planet. Sci. Lett.* **29,** 189–193.

McKenzie, D. P. (1978). Active tectonics of the Alpine–Himalayan belt: The Aegean Sea and surrounding regions, *Geophys. J. Roy. Astron. Soc.* **55,** 217–254.

Meghraoui, M., Z. Cakir, F. Masson, M. Ferry, S. Ergintav, S. Inan, V. Karabacak, and E. Altunel (2009). Active tectonics and kinematic modelling at the triple junction between the East Anatolian fault, the Dead Sea fault and the Cyprus arc, *Eos Trans. AGU* (Fall Meet.), Abstract G33D–0669.

Meghraoui, M., Z. Cakir, F. Masson, Y. Mahmoud, S. Ergintav, A. Alchalbi, S. Inan, M. Daoud, O. Yonlu, and E. Altunel (2011). Kinematic modelling at the triple junction between the Anatolian, Arabian, African plates (NW Syria and in SE Turkey), *Geophys. Res. Abstr.* **13,** Abstract EGU2011-12599.

Menekşe, A. (2016). Probabilistic seismic hazard assessment for East Anatolian fault zone using planar source models, *Master's Thesis*, Middle East Technical University, Ankara, Turkey.

Pacific Gas & Electric Company (PG&E) (2010). Verification of PSHA Code Haz43, *GEO.DCPP.10.03 Rev 0*.

Perinçek, D., and I. Çemen (1990). The structural relationship between the East Anatolian and Dead Sea fault zones in southeastern Turkey, *Tectonophysics* **172,** 331–340.

Perinçek, D., Y. Günay, and H. Kozlu (1987). New observations on strike-slip faults in east and southeast Anatolia, *Proc. of the 7th Petroleum Congress of Turkey*, Ankara, Turkey, 89–103.

Power, M., B. Chiou, N. Abrahamson, Y. Bozorgnia, T. Shantz, and C. Roblee (2008). An overview of the NGA project, *Earthq. Spectra* **24,** 3–21.

Reasenberg, P. (1985). Second-order moment of central California seismicity, 1969–82, *J. Geophys. Res.* **90,** 5479–5495.

Reilinger, R., S. McClusky, P. Vernant, S. Lawrence, S. Ergintav, R. Cakmak, H. Özener, F. Kadirov, İ. Guliev, R. Stepanyan, *et al.* (2006). GPS constraints on continental deformation in the Africa-Arabia-Eurasia continental collision zone and implications for the dynamics of plate interactions, *J. Geophys. Res.* **111,** doi: 10.1029/2005JB004051.

Şaroğlu, F., and Y. Yılmaz (1990). *Tectonics of the Karlıova Triple Junction*, Bulletin of ITU, Istanbul, Turkey.

Şaroğlu, F., O. Emre, and I. Kuscu (1992). The East Anatolian fault zone of Turkey, *Ann. Tecton.* **VI,** 99–125.

Scherbaum, F., N. M. Kuehn, M. Ohrnberger, and A. Koehlerb (2010). Exploring the proximity of ground-motion models using high-dimensional visualization techniques, *Earthq. Spectra* **26,** 1117–1138.

Stewart, J. P., J. Douglas, M. Javanbarg, Y. Bozorgnia, N. A. Abrahamson, D. M. Boore, K. W. Campbell, E. Delavaud, M. Erdik, and P. J. Stafford (2015). Selection of ground motion prediction equations for the Global earthquake model, *Earthq. Spectra* **31,** 19–45.

Taymaz, T., H. Eyidoğan, and J. Jackson (1991). Source parameters of large earthquakes in the East Anatolian fault zone (Turkey), *Geophys. J. Int.* **106,** 537–550.

Turkish Earthquake Code (2007). *Specification for Structures to be Built in Disaster Areas*, Ministry of Public Works and Settlement, Ankara, Turkey.

Utsu, T. (1965). A method for determining the value of b in a formula log $n = a - bM$ showing the magnitude–frequency relation for earthquakes, *Geophys. Bull. Hokkaido Univ.* **13,** 99–103.

Vakilinezhad, M., M. Levendoğlu, Z. Gülerce, and F. Şaroğlu (2013). Effect of fault characteristics on the probabilistic seismic hazard assessment results, *Proc. of International Conference on Earthquake Engineering*, Skopje, Macedonia, 29–31 May 2013.

Walling, M., W. Silva, and N. Abrahamson (2008). Nonlinear site amplification factors for constraining the NGA models, *Earthq. Spectra* **24,** no. 1, 243–255.

Weichert, D. (1980). Estimation of the earthquake recurrence parameters for unequal observation periods for different magnitudes, *Bull. Seismol. Soc. Am.* **70,** 1337–1346.

Wells, D. L., and K. J. Coppersmith (1994). New empirical relationships among magnitude, rupture length, rupture width, rupture area, and surface displacement, *Bull. Seismol. Soc. Am.* **84,** 974–1002.

Westaway, R. (2003). Kinematics of the Middle East and eastern Mediterranean updated, *Turkish J. Earth Sci.* **12,** 5–46.

Westaway, R. (2004). Kinematic consistency between the Dead Sea fault zone and the Neogene and Quaternary left-lateral faulting in SE Turkey, *Tectonophysics* **391,** 203–237.

Westaway, R. O. B., and J. A. N. Arger (1996). The Gölbaşi basin southeastern Turkey: A complex discontinuity in a major strike-slip fault zone, *J. Geol. Soc. Lond.* **153,** 729–744.

Wiemer, S. (2001). A software package to analyze seismicity: ZMAP, *Seismol. Res. Lett.* **72,** 373–382.

Wiemer, S., and M. Wyss (1997). Mapping the frequency–magnitude distribution in asperities: An improved technique to calculate recurrence times? *J. Geophys. Res.* **102,** no. B7, 15,115–15,128.

Woessner, J., L. Danciu, D. Giardini, H. Crowley, F. Cotton, G. Grünthal, G. Valensise, R. Arvidsson, R. Basili, M. N. Demircioglu, *et al.* (2015). The 2013 European seismic hazard model: Key components and results, *Bull. Earthq. Eng.* **13,** 3553–3596.

Woodcock, N. H., and M. Fischer (1986). Strike-slip duplexes, *J. Struct. Geol.* **8,** 725–735.

Working Group on California Earthquake Probabilities (WGCEP) (2003). Earthquake probabilities in the San Francisco Bay region: 2002–2031, *U.S. Geol. Soc. Open-File Rept. 03–214*.

Yalçınkaya, E. (2005). Stochastic finite-fault modeling of ground motions from the June 27, 1998 Adana-Ceyhan earthquake, *Earth Planets Space* **57,** 107–115.

Yılmaz, H., S. Över, and S. Özden (2006). Kinematics of the East Anatolian fault zone between Turkoğlu (Kahramanmaraş) and Celikhan (Adiyaman), eastern Turkey, *Earth Planets Space* **58,** 1463–1473.

Youngs, R. R., and K. J. Coppersmith (1985). Implications of fault slip rates and earthquake recurrence models to probabilistic seismic hazard estimates, *Bull. Seismol. Soc. Am.* **75,** 939–964.

Zimmaro, P., and J. P. Stewart (2017). Site-specific seismic hazard analysis for Calabrian dam site using regionally customized seismic source and ground motion models, *Soil Dynam. Earthq. Eng.* **94,** 179–192.

Department of Civil Engineering
Middle East Technical University (METU)
Ankara 06800, Turkey
zyilmaz@metu.edu.tr
ocetin@metu.edu.tr
(Z.G., K.Ö.Ç.)

Department of Geological Engineering
Middle East Technical University (METU)
Ankara 06800, Turkey
ozacar@metu.edu.tr
stshah.geo@gmail.com
kaymakci@metu.edu.tr
(S.T.S., A.A.Ö., N.K.)

Turkish-German University (TAU)
Istanbul 34820, Turkey
menekse@tau.edu.tr
(A.M.)

Manuscript received 10 January 2017;
Published Online 25 September 2017